Catalysis Communications 187 (2024) 106885

Contents lists available at ScienceDirect

Catalysis Communications

journal homepage: www.elsevier.com/locate/catcom

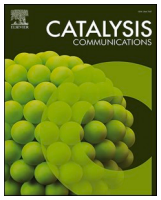

# AgNi/PC bimetallic and AgNi/PC@Mn trimetallic nanocatalysts for the efficient reduction of 4-nitrophenol

Hikmet Beyza Erdem, Sevil Çetinkaya *

*Kirikkale University, Department of Chemistry, 71450 Yahsihan, Kirikkale, Türkiye*

ARTICLE INFO

*Keywords:*
Trimetallic catalyst
Nanocatalyst
4-nitrophenol
Catalytic reduction
Porous carbon

ABSTRACT

Catalytic efficiency in hydrogenation reactions can be increased due to the stability achieved with nanomaterials prepared by homogeneously immobilizing multiple metal nanoparticles onto porous solid materials. Herein, porous carbon (PC)-supported bimetallic (AgNi/PC) and trimetallic nanoparticles (AgNi/PC@Mn) were developed and evaluated as catalysts in the $NaBH_4$-mediated reduction of 4-nitrophenol to 4-aminophenol. AgNi/PC@Mn catalysts were synthesized using a two-step synthesis strategy. The highest and excellent catalytic efficiency under ambient conditions was obtained by the trimetallic catalyst. Both catalysts proved to be easily separated from the reaction medium and usable for up to five consecutive cycles without losing their catalytic activity.

## 1. Introduction

Nitrophenols are dangerous pollutants causing water pollution due to their high solubility and stability in the aqueous environment [1]. These compounds are commonly used in the production of hazardous materials (e.g., dyes, drugs, insecticides, herbicides, fungicides, and explosives) [2]. Nitrophenol-containing wastes are discharged into the environment in large quantities through agricultural uses and medical applications. 4-Nitrophenol (4-NP) is a hazardous chemical that can easily cause inflammation and allergies on the skin and is also resistant to hydrolysis, chemical, and biological oxidation as it has a strong electron-withdrawing nitro group [3,4]. Therefore, the development of environmentally friendly techniques is necessary for the removal of nitrophenols from industrial wastewater [5]. The most suitable method, chemical reduction, offers significant advantages such as low cost, shorter reaction time, and high conversion [6]. Additionally, aminophenol obtained as a result of the chemical reduction of nitrophenols is a less toxic compound and is also used as a precursor for corrosion inhibitors, drying agents, photographic developer for films, fire suppressants, and analgesic synthesis [7]. Reducing agents, such as $NaBH_4$ and metal nanoparticles (NPs), are used as suitable reagents and catalysts to convert 4-NP to 4-aminophenol (4-AP).

Metal NPs are classified as mono, bi, tri, or poly-metallic NPs, depending on the number of metal components they contain [8]. Multimetallic NPs, including bimetallic and trimetallic NPs, have gained significant attention due to their unique optical, electronic, chemical, and catalytic properties [9]. Nano-sized bimetallic NPs can be highly active catalysts with significantly improved activity and selectivity compared to their monometallic counterparts [10]. By adding a noble metal to a transition metal, the electrical density of the transition metal increases, so the NPs can be more effective catalysts [11]. Additionally, their stability and lower susceptibility to aggregation and deactivation during catalytic processes make them superior to monometallic NPs [12]. For instance, bimetallic Ag—Ni, Au—Pd, Au—Pt, Au—Rh, and Pt—Ru NPs show higher catalytic performance compared to their monometallic counterparts [13]. AgNi NPs, in particular, have attracted great attention due to the unique combinations of noble and non-noble metals. Ag is preferred over other noble metals due to its high electronic conductivity, antimicrobial properties, catalytic activity, and chemical stability [14]. Nickel, on the other hand, is highly sought-after for its excellent catalytic properties, abundant availability, low cost, and high electrochemical stability [15]. Ni is also a transition metal with high catalytic activity, magnetism, and corrosion resistance. Numerous studies have shown that Ni exhibits similar catalytic performance to the valuable metal Pd due to its similar electronic structure [16].

In catalytic applications, trimetallic NPs exhibit better catalytic activity and selectivity compared to bimetallic and monometallic NPs, primarily due to the combination of properties between the first metal with the second and third metals [17,18]. The addition of cheap metals with low catalytic activity to expensive metals with important catalytic

* Corresponding author.
*E-mail address:* scetinkaya@kku.edu.tr (S. Çetinkaya).

https://doi.org/10.1016/j.catcom.2024.106885
Received 6 November 2023; Received in revised form 17 February 2024; Accepted 21 February 2024
Available online 23 February 2024
1566-7367/© 2024 The Authors. Published by Elsevier B.V. This is an open access article under the CC BY license (http://creativecommons.org/licenses/by/4.0/).

properties reduces the production cost and increases the activity of the prepared catalysts [19]. Trimetallic NPs can be synthesized using various methods, including microwave, catalytic reduction, microemulsion, co-precipitation, hydrothermal, sol-gel, and seed-mediated growth [20].

Due to their large surface areas, bimetallic and trimetallic NPs have high surface energy, and so during and after synthesis, nanoparticles tend to agglomerate and reduce their surface areas. NPs aggregate without repulsive forces created by electrostatic or steric stabilization [21]. However, despite using the best stabilizers, nanoparticle agglomeration cannot be completely prevented. Therefore, NPs are usually immobilized on a solid support [22]. Support materials not only facilitate the removal of the catalyst from the reaction but also act as a conductive bridge that connects nanoparticles to the external environment, thus enhancing their catalytic performances [23]. Commonly used solid supports include silica, metal oxides, carbon materials, porous carbon, graphene oxide, and zeolites. Porous carbon is preferred over oxides and other supports due to its low cost, stability in acidic and basic environments, porosity for certain catalytic applications, adjustable specific surface area, and surface chemistry [24]. Although porous carbon can be produced from many carbon-based materials, it has been recently reported by our research group that highly porous carbons with super-porous carbon properties can be obtained from petroleum asphaltene [25].

The catalytic effect of AgNi nanoparticles has attracted attention recently. However, there are very few studies on supported AgNi nanoparticles and no report on AgNi and AgNiMn nanoparticle-supported asphaltene-based porous carbons [26–30]. Taking into account recent positive developments, we have designed new bimetallic and trimetallic reusable nanocatalysts supported on asphaltene-derived porous carbon for the first time. Due to the superior properties of the mentioned bimetallic nanoparticles, manganese was chosen as a cheap, non-toxic, and catalytic material to obtain trimetallic nanoparticles. Both of the new catalysts exhibited high surface areas. The catalytic performance of the resultant catalysts was investigated in detail. Porous carbon-supported trimetallic catalyst showed higher catalytic activity compared to bimetallic catalyst.

## 2. Material and methods

### 2.1. Instruments and materials

Manganese (ll) acetylacetonate ($Mn(acac)_2$, Mn, 21.0–23.0% EDTA titration), nickel (ll) acetylacetonate ($Ni(acac)_2$, 95%), KOH, $AgNO_3$, 1-octadecene, oleylamine (OAm, technical grade, 70%), HCl, acetone, hexane, and n-heptane were bought from Sigma Aldrich. 4-NP and $NaBH_4$ were obtained from Merck. All reagents were used in analytical and spectral purity grades (unless specified) without any further purification. Asphaltene-derived carbon (PC) with a specific surface area of 2276 $m^2/g$ used as a support material was previously synthesized and characterized [31]. XRD patterns were recorded on a Rigaku Ultima-IV X-ray diffractometer using *Cu* Kα *radiation* ($\lambda = 1.5406$ *Å)* operating at *40 kV,* and *30 mA*. $N_2$ adsorption-desorption isotherms of the synthesized nanoparticles were carried out on a surface area and pore size analyzer (Quantachrome Corporation Autosorb-6B). BET (Brunauer-Emmett-Teller), DFT (density-functional theory), and t-plot method were applied to the analysis. A field emission scanning electron microscope (FESEM, FEI Quanta 400F) and a high-contrast transmission electron microscope (CTEM, FEI TEM Tecnai G2 Spirit Biotwin) were used to obtain the SEM and TEM images, respectively. Elemental concentrations were determined by a PerkinElmer DRC II inductively coupled plasma-optical emission spectrometer (ICP-OES). TGA analysis of the synthesized nanoparticles was performed with a Perkin Elmer Pyris-1 model thermogravimetric analyzer under $N_2$ gas at a heating rate of 10 °C/min and a temperature range of 25–900 °C. Catalytic performances were monitored and determined by a UV–Vis spectrophotometer (SHIMADZU UV-1800).

### 2.2. Synthesis of AgNi/PC NPs

A similar procedure was used for the synthesis of AgNi/PC NPs [32]. Briefly, 0.5 g of PC, equimolar amounts (0.3 mmol) of $AgNO_3$ and Ni $(acac)_2$ were mixed with 20 mL of OAm at room temperature. The temperature of the resultant mixture was increased to 80 °C during the 20-min period under reflux conditions. Then the temperature was increased to 180 °C and mixed at this temperature for an additional 3 h. After the solution was allowed to cool to room temperature, 40 mL of acetone/hexane (1:1, v:v) was added and centrifuged at 9000 rpm for 15 min. This process was repeated three times. The resulting nanoparticle (named AgNi/PC) was finally dried in a vacuum oven at 25 °C for 24 h.

### 2.3. Synthesis of AgNi/PC@Mn NPs

The synthesized AgNi/PC was suspended in 5 mL of hexane. 3 mL of the suspended solution was added dropwise to the mixture of 0.1 mmol of $Mn(acac)_2$ and 10 mL of 1-octadecene. The temperature of the mixture was increased to 100 °C under reflux conditions and stirred at this temperature for 30 min. Then the solution temperature was increased to 200 °C at a heating rate of 1 °C/min and kept at this temperature for an additional 3 h. After the solution was allowed to cool to room temperature, 20 mL of acetone/hexane (1:1, v:v) was added and centrifuged at 9000 rpm for 15 min. This process was repeated three times. The resulting nanoparticle (named AgNi/PC@Mn) was finally dried in a vacuum oven at 25 °C for 24 h.

### 2.4. Catalytic performance in hydrogenation reactions

The effect of catalysis parameters such as time, catalyst dosage, and initial concentrations of 4-NP on the reduction efficiency was thoroughly investigated. In catalytic studies, the progress of the *reduction of 4-NP* was monitored by taking absorbance measurements at 400 nm wavelength. In a typical reduction reaction, an aqueous $NaBH_4$ solution (0.5 M, 10 mL) and the catalyst (30 mg) were added to 100 mL of 4-NP solutions (0.1–0.5 mmol/L) and stirred at room temperature. To study the effect of catalyst dosage, 100 mL of 0.10 mmol/L 4-NP and 10 mL of 0.5 M $NaBH_4$ solution were used by changing the amount of catalyst from 10 mg to 130 mg. 3 mL of the suspension was taken out at regular intervals, filtered, and subjected to UV–Vis analysis. The percentage of 4-NP removal (E%) was determined by using the following Eq. (1):

$$E(\%) = [(Ao–At)/Ao] \times 100\% \quad (1)$$

where $A_o$ and $A_t$ represent the initial absorbance of nitrophenol and the absorbance of nitrophenol at time t, respectively.

## 3. Results and discussion

AgNi/PC@Mn NPs were synthesized by a one-pot and two-step strategy. In the first step, AgNiNPs on PC were synthesized in oleylamine, which served as both an equalizer of the decomposition temperatures and a solvent [33]. Both precursors, $AgNO_3$ and $Ni(acac)_2$, were decomposed at similar temperatures to form bimetallic nanoparticles. In the next step, AgNi/PC@Mn NPs with a trimetallic structure were successfully synthesized by the seed-initiated growth method in 1-octadecene by using the synthesized AgNi/PC NPs as seed. The X-ray diffractogram of AgNi/PC NPs is presented in Fig. 1. The broad diffraction peak at around $2\theta = 21°$ assigned to the (002) plane confirmed that PC was amorphous [34]. Both Ni and Ag nanoparticles *formed face-centered cubic (fcc) lattices*. Diffraction peaks in Fig. 1 were indexed to Ag (111), Ag (200), Ni (111), Ag (220), Ni (222), and Ag (311) planes of *fcc*-Ag and NiNPs fabricated on PC matrix (ICDD No. 00-

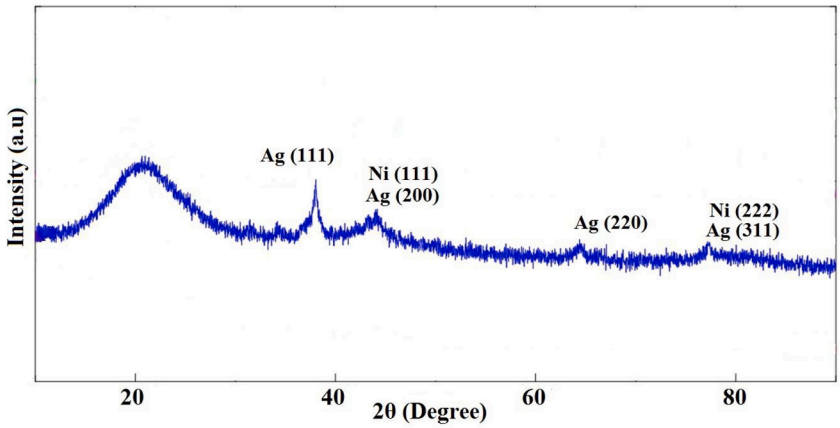


**Fig. 1.** XRD pattern of AgNi/PC NPs.

04-0783; ICDD No. 00-04-0850) [35]. It should be noted that the characteristic peaks for the (111) and (222) lattice planes of Ni NPs with a fcc structure possibly overlapped with peaks correspond to the (200) and (311) planes of Ag [36]. The crystallite size of the bimetallic nanoparticle supported on PC was obtained as 15.1 nm from the (111) diffraction peak using Scherrer's equation, where peak position and full width at half maximum (FWHM) in degrees were 38.047 and 0.58, respectively. The surface properties of AgNi/PC NPs were analyzed via nitrogen adsorption-desorption isotherms and the corresponding pore size distribution curves (Fig. 2a). BET area value of 211 $m^2/g$ and a micropore area of 89 $m^2/g$ were determined for this nanoparticle using the BET- and t-plot method micropore analyses, respectively. The pore size and total pore volume for AgNi/PC NPs using the DFT model were found to be 1.4 nm and 0.13 $cm^3/g$, respectively. AgNi/PC NPs had a maximum nitrogen uptake of 86 $cm^3/g$. As illustrated in Fig. 2b, AgNi/PC NPs exhibited adsorption isotherms of type I(c). The type I(c) isotherm was considered to be a combination of the type I(b), II, and IV (a) isotherms of IUPAC, verifying that the material had both micro- and mesopores [37]. The presence of first and second peaks between 1 and 5 nm revealed that the sample contains micropores (<2 nm) and mesopores (mostly <5 nm), respectively.

The surface morphology of AgNi/PC NPs and the presence of metal nanoparticles were analyzed using recorded FESEM and EDX spectra (Fig. 3). *Non-agglomerated* Ag (darker spots) and Ni (lighter spots) NPs were distributed uniformly on the surface and inside the pores of carbon. The appearance of the darker and lighter spots was due to the large difference in the electron scattering abilities of Ag and Ni. The large pores of the carbon structures were homogeneously covered with AgNi NPs. The EDX spectrum obtained during the FESEM analysis confirmed the presence of Ag and Ni metals as well as carbon elements. Due to the presence of asphaltene-derived carbon in the material, the peaks belonging to C$K_\alpha$, O$K_\alpha$, and S$K_\alpha$ were observed at 0.22, 0.54, and 2.30 keV, respectively [38]. The EDX spectrum represented the presence of an elementary component of the silver nanoparticles, with 2.82, 2.96, 3.17, and 3.45 keV corresponding to the binding energies of Ag$L_1$, Ag$L_\alpha$, Ag$L_\beta$, and Ag$L_\gamma$, respectively [39]. In the EDX spectrum, four Ni peaks were observed at 0.81, 0.89, 7.65 keV, and 8.29 keV, which belong to $L_1$, $L_\alpha$, $K_\alpha$ and $K_\beta$ emission, respectively [38].

The histograms of nanoparticle diameters prepared by analyzing micrographs of AgNi NPs with the ImageJ program are given in Fig. 4. The CTEM images of AgNi NPs on PC revealed that the nanoparticles had a mean particle size of 14.58 nm. The selected area electron diffraction (SAED) pattern of AgNi/PC NPs confirmed the presence of polycrystalline nanoparticles (Fig. 4c). The rings were assigned to the fcc structure of Ag and Ni NPs [27]. According to ICP-OES analysis, the silver and nickel contents were 0.97% ± 0.01 and 1.11% ± 0.1, respectively.

AgNi/PC@Mn NPs were obtained by the direct seed-mediated growth method by adding a solution containing bimetallic nanoparticles to Mn precursors in 1-octadecene solvent medium. The XRD pattern of a trimetallic nanoparticle is presented in Fig. 5. The broad XRD peak centered at 2θ = 20.75° was assigned to the (002) plane of PC support [40]. The peaks at 2θ = 37.99°, 44.21°, 64.33°, 77.27°, and 81.5° belong to the (111), (200), (220), (311), and (222) fine crystal planes of fcc-structured Ag in AgNi/PC@Mn NPs (ICDD: 01–087-0597) [41]. Trimetallic and bimetallic NPs showed nearly the same XRD peaks,

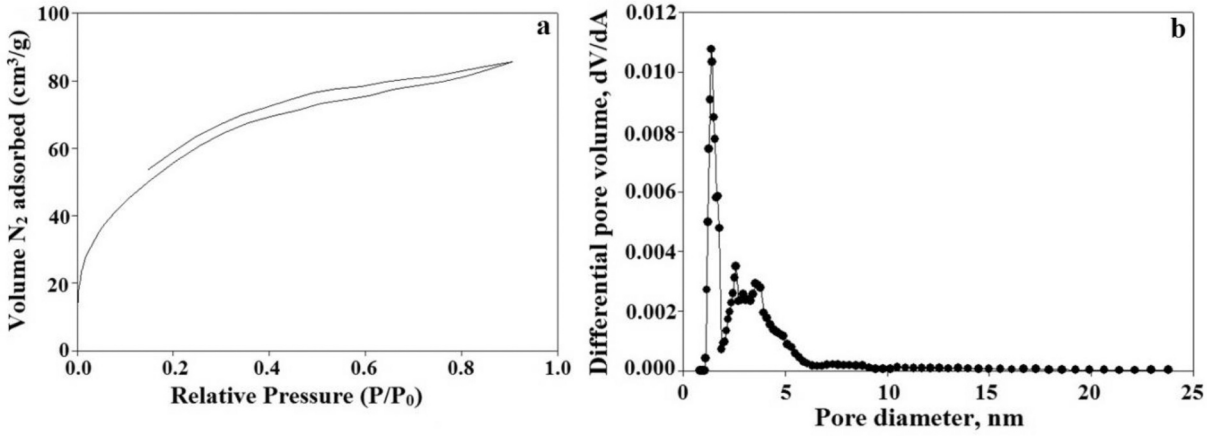


**Fig. 2.** (a) Nitrogen adsorption–desorption isotherm, and (b) corresponding DFT pore size distribution curve for AgNi/PC NPs.

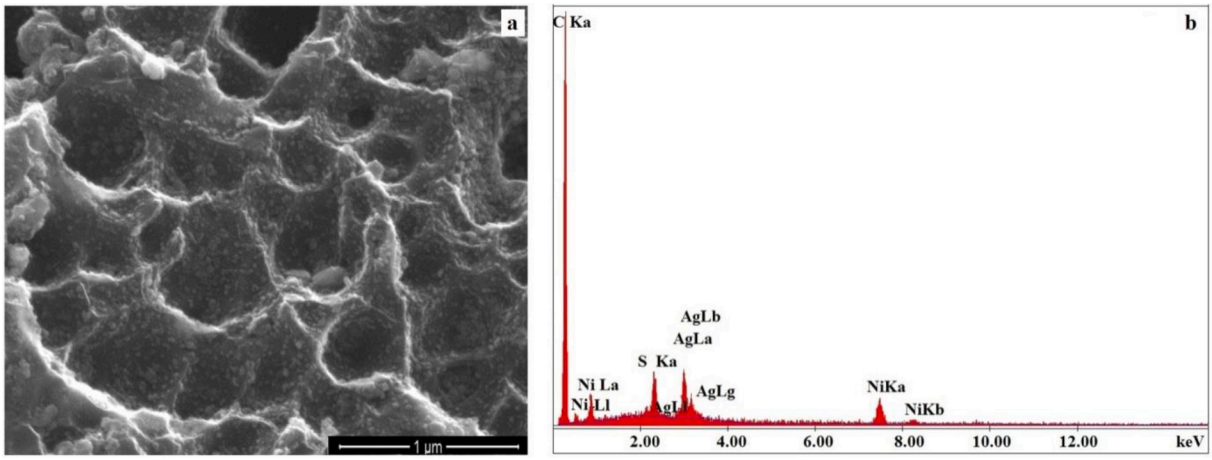


**Fig. 3.** (a) FESEM image, and (b) EDX spectrum for AgNi/PC NPs.

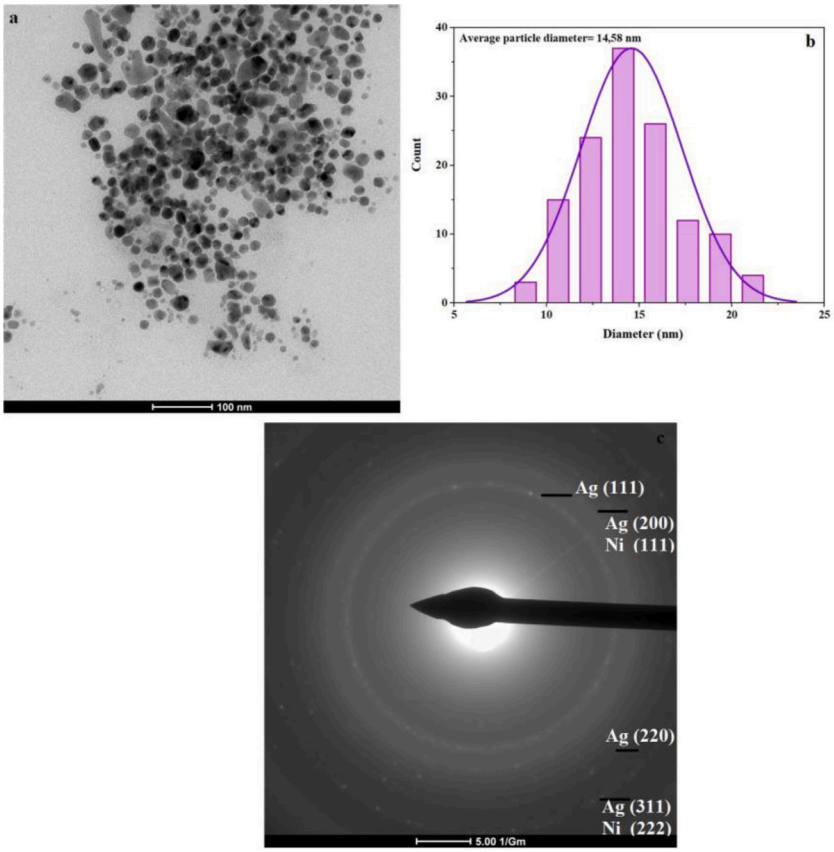


**Fig. 4.** (a) TEM image, (b) particle distribution histogram graph, and (c) SAED pattern for AgNi/PC NPs.

indicating the addition of a low amount of Mn did not change the fcc structures of the trimetallic nanoparticle. The average crystallite size of the nanoparticles based on the (111) reflection was calculated to be 18.2 nm by the Scherer equation.

The nitrogen adsorption-desorption isotherm and pore size distribution curve of AgNi/PC@Mn NPs are displayed in Fig. 6. AgNi/PC@Mn NPs showed a type I(c) isotherm, characteristic of systems containing micro- and macroporous. The hysteresis loop in the range of 0.4–0.9 was consistent with the H4-shaped hysteresis [37]. The DFT pore size distribution curve showed the nanoparticles are mainly microporous, giving a microporous surface area of 1246 $m^2/g$. The micropore surface area of the catalyst accounted for 80% of the total surface area. When Mn nanoparticles were loaded onto AgNi/PC, the BET surface area increased from 211 $m^2/g$ to 1562 $m^2/g$ for AgNi/PC@Mn nanoparticles, and the pore volume also increased from 0.13 to 0.85 $cm^3/g$. The sharp increase in BET surface area might be due to the newly formed microporous structures. The mean pore size of AgNi/PC@Mn NPs was 1.3 nm. While the maximum $N_2$ adsorption amount of bimetallic nanoparticles was 86 $cm^3/g$, that of AgNi/PC@Mn trimetallic nanoparticles reached a maximum of 564 $cm^3/g$, as expected.

Fig. 7a shows the FESEM image of the AgNi/PC@Mn NPs. From the image, it is apparent that the pore structure observed in bimetallic nanoparticles disappeared and the large pores were homogeneously coated with manganese nanoparticles. The EDX spectrum given in

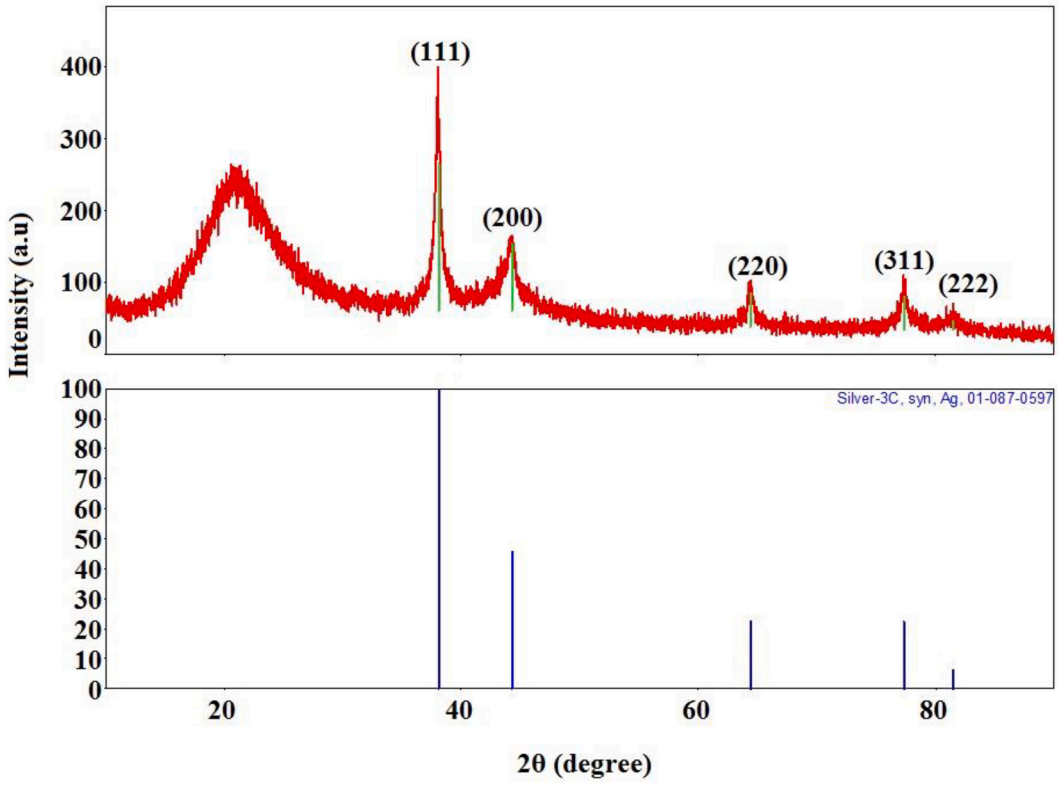


**Fig. 5.** XRD pattern of AgNi/PC@Mn NPs.

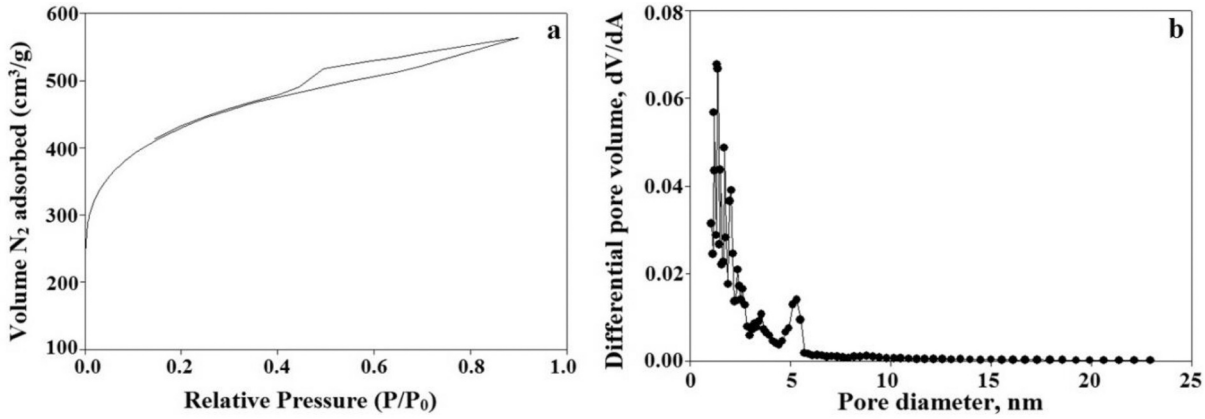


**Fig. 6.** (a) Nitrogen adsorption–desorption isotherm, and (b) corresponding pore size distribution curve for AgNi/PC@Mn NPs.

Fig. 7b confirmed that the AgNi/PC@Mn NPs mainly included C, Ag, Ni, and Mn. The peaks at 2.82, 3.00, 3.18, and 3.36 keV corresponding to Ag$L_1$, Ag$L_\alpha$, Ag$L_\beta$, and Ag$Ly$ were observed [40]. EDX spectral bands were observed at 7.65 keV ($K_\alpha$) and 8.29 keV ($K_\beta$) for Ni nanoparticles [39]. In addition to the EDX signals observed in AgNi/PC NPs, the signals at 5.81 keV (for Mn$K_\alpha$) and 6.45 keV (for Mn$K_\beta$) for trimetallic nanoparticles were due to the presence of manganese [42,43]. The TEM image and particle size distribution

histograms given in Fig. 8a and b proved the average size of the nanoparticles to be 15.16 nm. The SAED pattern (Fig. 8c) also confirmed the presence of 'fcc' structured metallic silver. ICP-OES analysis proved a loading of 2.2 ± 0.1 wt% Ag, 1.2 ± 0.1 wt% Ni, and 0.7 ± 0.01 wt% Mn.

PC-supported bimetallic and trimetallic nanoparticles were also characterized for their thermal decomposition behavior via thermogravimetric analysis (TGA), and the related thermograms are presented in Fig. 9. Although bimetallic NPs decomposed in a single step, Mn-containing trimetalic NPs decomposed in three stages. The total weight losses of AgNi/PC (Fig. 9a) and AgNi/PC@Mn (Fig. 9b) determined at around 200–500 °C were 27.5% and 1.25%, respectively. It was determined that the addition of Mn stabilized the AgNi/PC containing two metals and exhibited very stable thermal behavior at the same temperature ranges.

The performance of both catalysts (AgNi/PC and AgNi/PC@Mn) in reducing 4-NP to 4-AP was examined using a reducing agent, $NaBH_4$. The reduction efficiency of the bimetallic and trimetallic catalysts was monitored by employing UV–Vis spectroscopy. The UV spectrum of the 4-NP aqueous solution showed $\lambda_{max}$ at 317 nm (Fig. 10a). After the addition of $NaBH_4$, the absorbance peak shifted to 400 nm due to the formation of a 4-nitrophenolate ions ($4\text{-}NP^-$) (Fig. 10b) [44]. The reduction of 4-NP with $NaBH_4$ in the absence and presence of catalyst was performed and monitored until no more reaction was observed. As

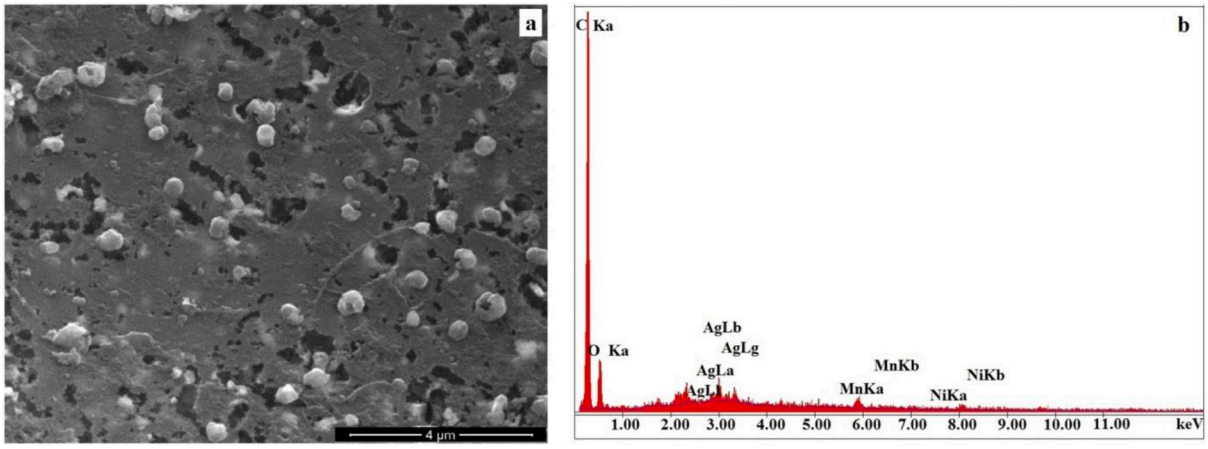


**Fig. 7.** (a) FESEM image, and (b) EDX spectrum for AgNi/PC@Mn NPs.

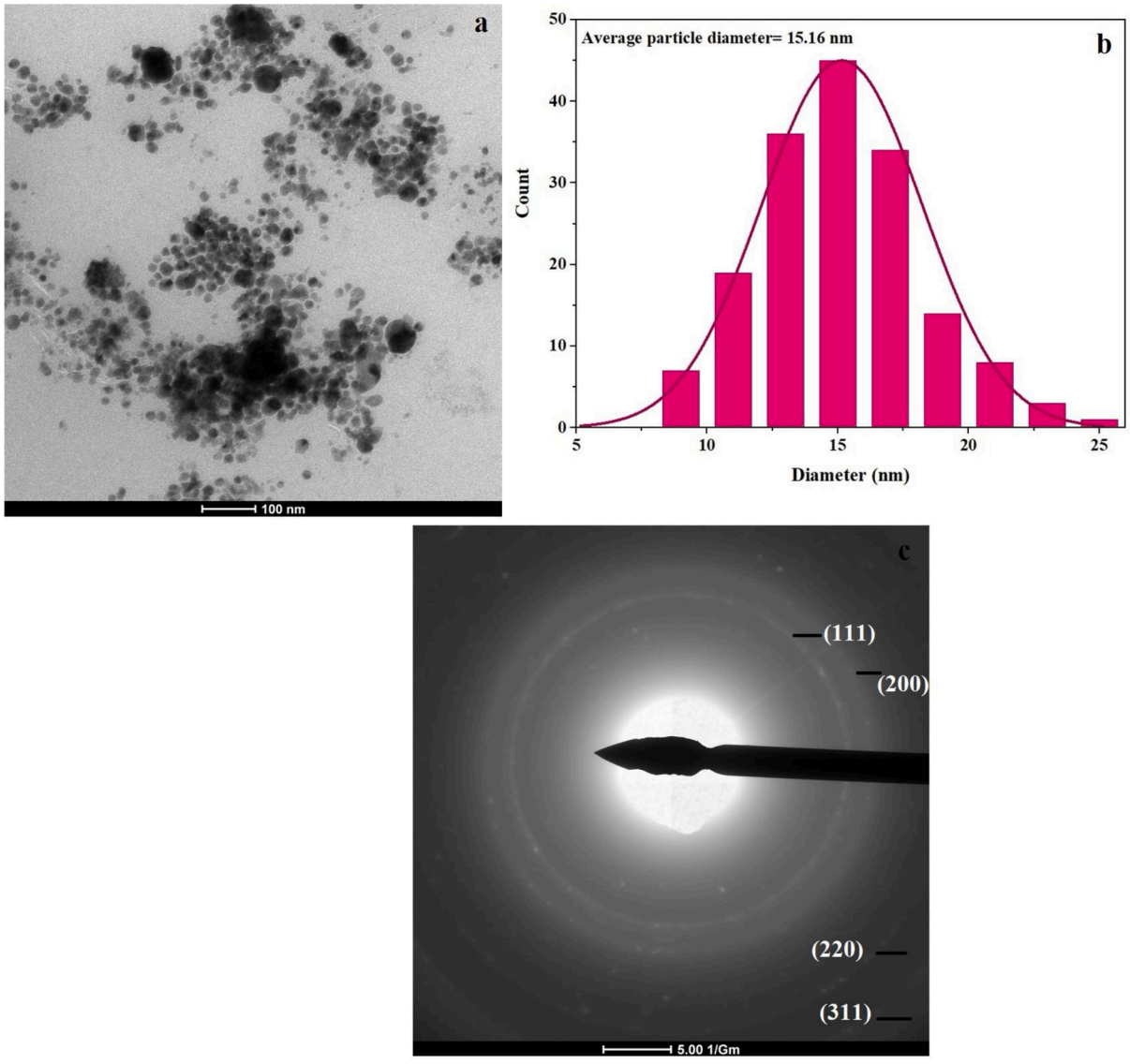


**Fig. 8.** (a) TEM image, (b) particle size distribution histogram, and (c) SAED pattern for AgNi/PC@Mn NPs.

presented in Fig. 10b, the reduction of 4-NP with catalyst-free $NaBH_4$ was quite weak due to the high kinetic barrier. By adding of AgNi/PC and AgNi/PC@Mn catalysts to the reaction solution, the absorbance intensity at 400 nm significantly decreased, and the simultaneous appearance of the new absorption peak at 300 nm corresponding to 4-AP was observed (Figs. 10c-d) [45].

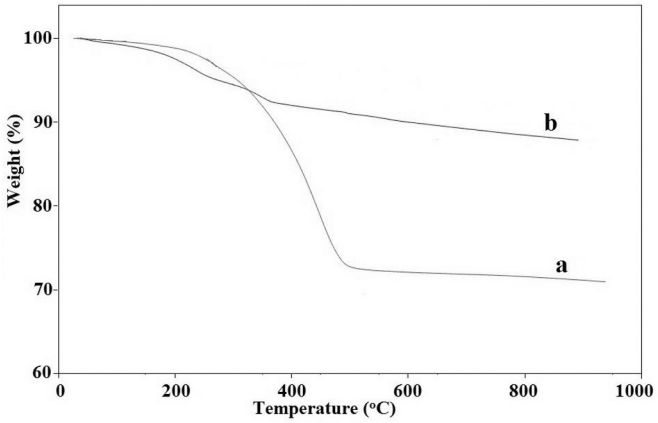


**Fig. 9.** TGA curves of (a) AgNi/PC NPs and (b) AgNi/PC@Mn NPs.

The effects of initial concentration, catalyst dosage, and reaction time on the reduction of 4-NP were studied. The pH value of a reaction medium greatly affects the catalysis rate. Therefore, researchers often study the catalytic reaction in buffer medium to achieve high conversion efficiencies. However, there is no constant pH value in industrial waste. Therefore, we preferred to carry out catalytic studies without creating any buffer medium and without pH adjustment. The removal efficiency of 4-NP at different initial concentrations was performed by using bimetallic and trimetallic catalysts with a 30 mg catalyst and a 0.5 M $NaBH_4$ solution. Figs. 11 and 12 show the kinetic plot of ln ($A_t/A_0$) vs. time for each of the catalysts tested. As can be seen from Fig. 11a, the time to reach the maximum conversion increased as the initial concentration increased. The reaction was found to be 87% complete in 8 min when the 4-NP concentration was 0.1 mmol/L by using a bimetallic catalyst. However, only 42% conversion was achieved with an initial 4-NP concentration of 0.5 mmol/L in 8 min. Similarly, reduction efficiency with a trimetallic catalyst for 0.1 mmol/L and 0.5 mmol/L initial concentrations was 91% and 59% in 8 min, respectively (Fig. 12a). This is the result of the saturation of the nanoparticle surface with 4-NP molecules, resulting in a decrease in the rate of electron transfer to the nanoparticle surface [46]. In all cases, it was noted that the initial conversion rate for a trimetallic catalyst was higher than that for a bimetallic catalyst. Furthermore, 20 min and 16 min were required to achieve a complete conversion for bimetallic and trimetallic, respectively.

With the pseudo-first-order kinetic model, the reaction kinetic parameters were analyzed according to Eq. (2) given below:

$$ln\ A_t/A_0 = -k_1 t \quad (2)$$

where $k_1$ is the rate constant of the reaction. Rate constants were

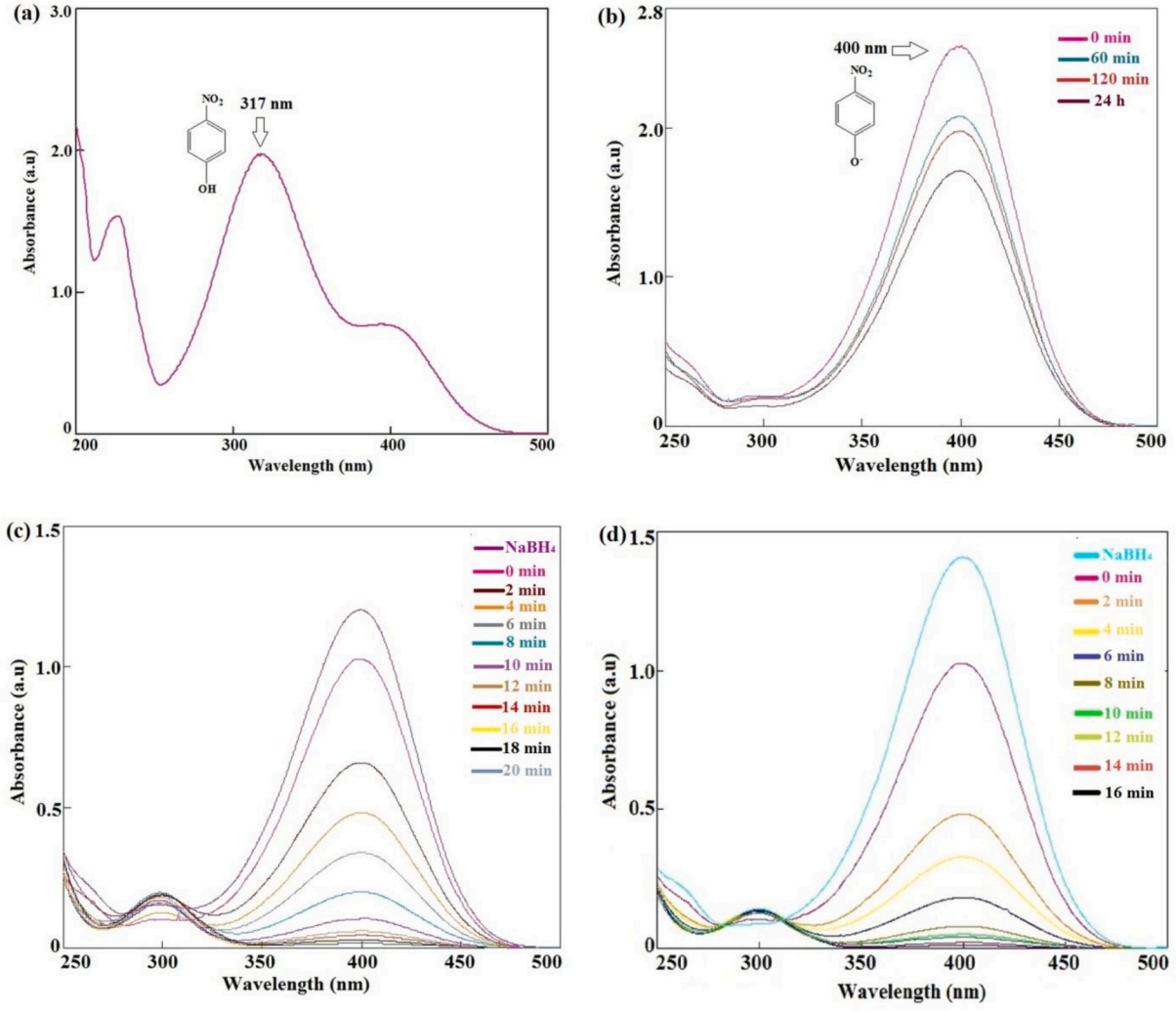


**Fig. 10.** (a) UV- Vis spectrum of 4-NP, (b) UV- Vis spectrum of 4-NP ion in the presence of $NaBH_4$, (c) Reduction of 4-NP in the presence of AgNi/PC NPs, (d) Reduction of 4-NP in the presence of AgNi/PC@Mn NPs at time intervals. [4-NP] = 0.1 mmol/L, [$NaBH_4$] = 0.5 M, $m_{cat}$ = 30 mg, solvent = $H_2O$, $T$ = 25 °C.

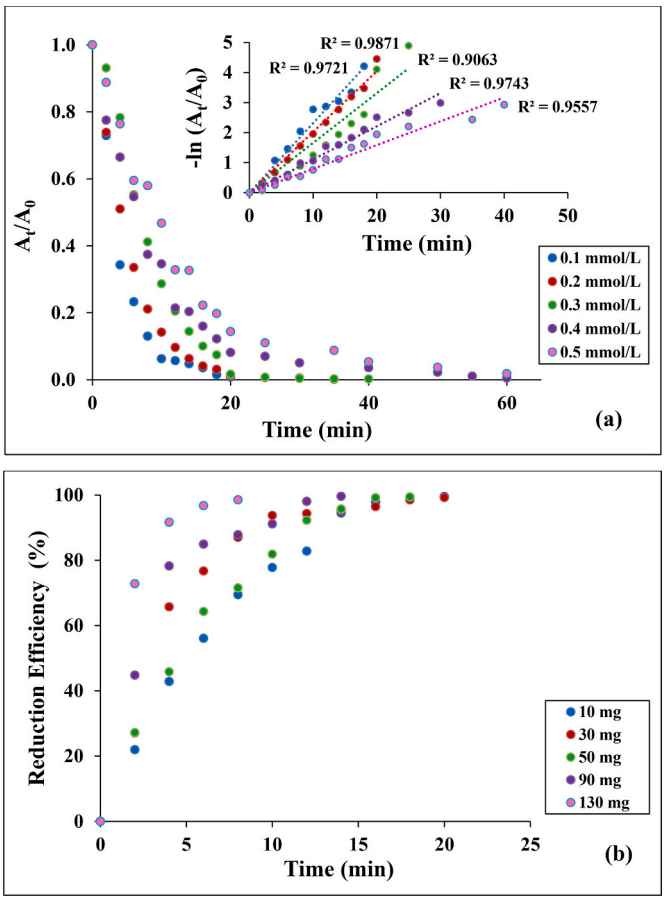


**Fig. 11.** (a) Effect of initial phenol concentration on the reduction of 4-NP and plots of ln ($A_t/A_0$) versus reaction time, (b) Effect of catalyst loading on the reduction of 4-NP with AgNi/PC catalyst.

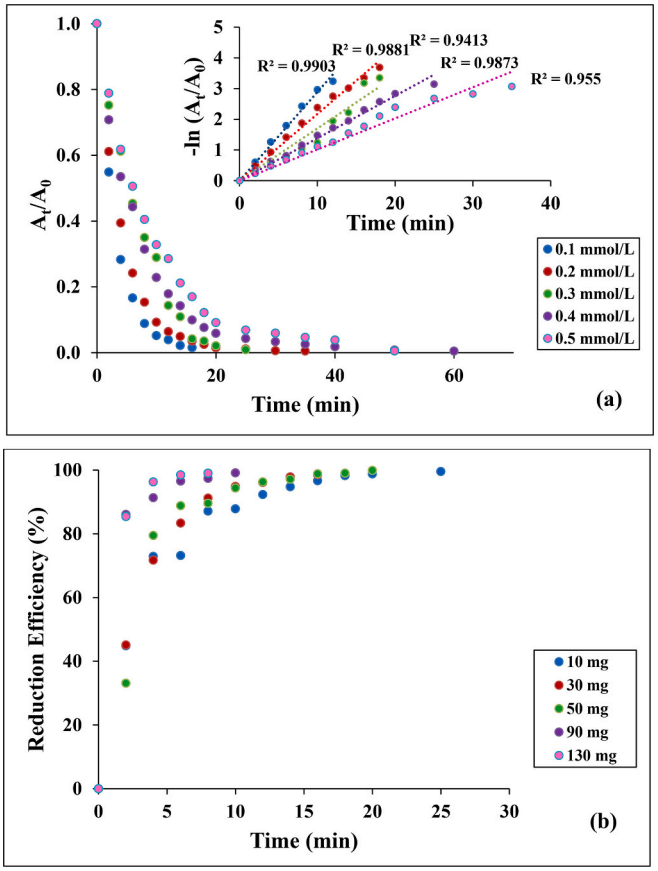


**Fig. 12.** (a) Effect of initial phenol concentration on the reduction of 4-NP and plots of ln ($A_t/A_0$) versus reaction time, (b) Effect of catalyst loading on the reduction of 4-NP with AgNi/PC@Mn catalyst.

determined from the *slope* of the straight *line obtained* by the *graph* of *ln* $A_t/A_o$ vs. *time*. The kinetic studies showed that the 4-NP catalytic reduction performed with bimetallic and trimetallic catalysts followed the pseudo-first-order with a rate constant of 0.2315 and 0.2884 $min^{-1}$, respectively. The higher rate constant with trimetallic catalyst proves the synergistic properties of porous carbon, Ag, Ni and Mn nanoparticles. The rate constants of the reaction catalyzed by the bimetallic and trimetallic catalyst decreased to 0.0791 and 0.1014 $min^{-1}$, with the increase of 4-NP concentration from 0.1 to 0.5 mmol/L, respectively. As a result, it was determined that the trimetallic catalyst was quite active for 4-NP reduction as a natural result of the synergistic catalytic performance.

Plots of reduction efficiency (%) vs. time in min at different bimetallic and trimetallic catalyst dosages are shown in Figs. 11b and 12b. Increasing the catalyst dosage from 10 to 130 mg reduced the *time* required for the complete conversion. The fastest rate for 4-NP reductions was obtained with a dosage of 130 mg for both catalysts. A reduction efficiency of 73% was reached within the first 2 min when bimetallic catalyst was used as a catalyst. A reduction efficiency of only 22% was achieved when 10 mg of the same catalyst was used during this time. Similarly, when trimetallic catalyst was used as catalyst, a reduction efficiency of 86% was reached within the first 2 min and the complete conversion of 4-NP was achieved in 6 min with a rate constant of 0.7536 $min^{-1}$. In summary, porous carbon-based bimetallic and trimetallic nanocatalysts turned out to be comparable or more efficient than other reported bi- and trimetallic catalyst for 4-NP reduction, as seen in Table 1.

The mechanistic pathway for the reduction of 4-NP to 4-AP by $NaBH_4$ in the presence of catalysts can be described using different pathways. The decrease in the value of the reduction rate constant value as the 4-NP concentration increased showed that the reaction mechanism fit well with the Langmuir-Hinshelwood (LH) model (Fig. 13) [45]. According to this mechanism, adsorption of the borohydride ions to the catalyst surface occurs before the catalytic reaction, and a surface hydrogen species is transferred to the surface of the nanoparticles [47]. The rate-determining step is the reduction of nitro groups to amino groups by the reaction of adsorbed 4-NP with the hydrogen atoms formed on the surface of the bimetallic and trimetallic catalysts.

Evaluation of reusability is very important for examining the practical usability of newly discovered catalysts. In our case, the separation was readily achieved by filtration, and the long-term performance of the bimetallic and trimetallic catalysts was evaluated for five cycles (Fig. 14). Observing the 4-NP reduction efficiency of ~100% after five cycles proved the catalysts were stable and reusable. The *time* for *complete reduction* of 4-NP increased slightly as the number of cycles increased, partly due to aggregation. When the AgNi/PC catalyst was

**Table 1**
Comparison of the synthesized catalysts with other reported catalysts.

| Catalyst | Rate constant $k_1$ ($min^{-1}$) | Reaction time (min) | Reference |
|---|---|---|---|
| Ni@Cu@Pd NPs | 0.1100 | 3 | [48] |
| GK-AgAuPd NPs | 0.2870 | 10 | [49] |
| $Ag_2Au_1Pd_2$ NPs | 0.0466 | 20 | [50] |
| Ag-Fe NPs | 0.0312 | 45 | [51] |
| Au-Ag NPs | 0.0285 | 30 | [52] |
| $Ag_2Au_1Pd_4$ NPs | 0.0041 | 20 | [50] |
| AgNi/PC NPs | 0.2315 | 20 | This work |
| AgNi/PC@Mn NPs | 0.2884 | 16 | This work |

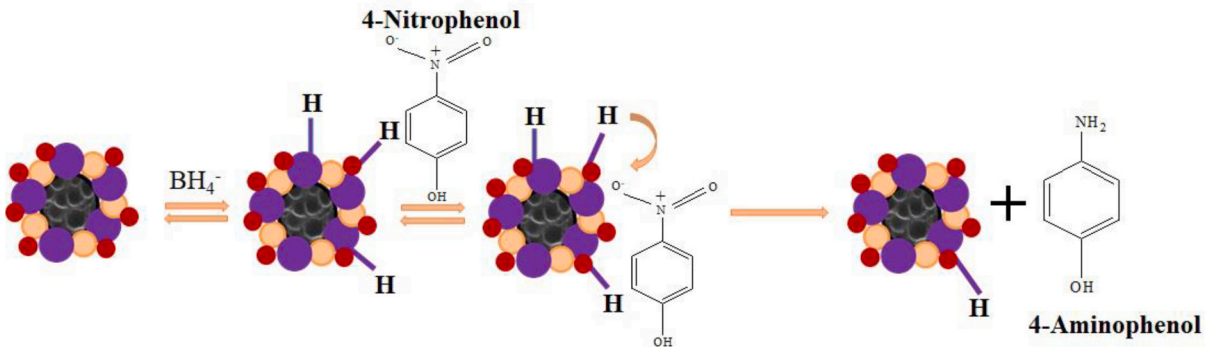


**Fig. 13.** Catalytic reduction of 4-NP on nanocatalyst surface in presence of $NaBH_4$.

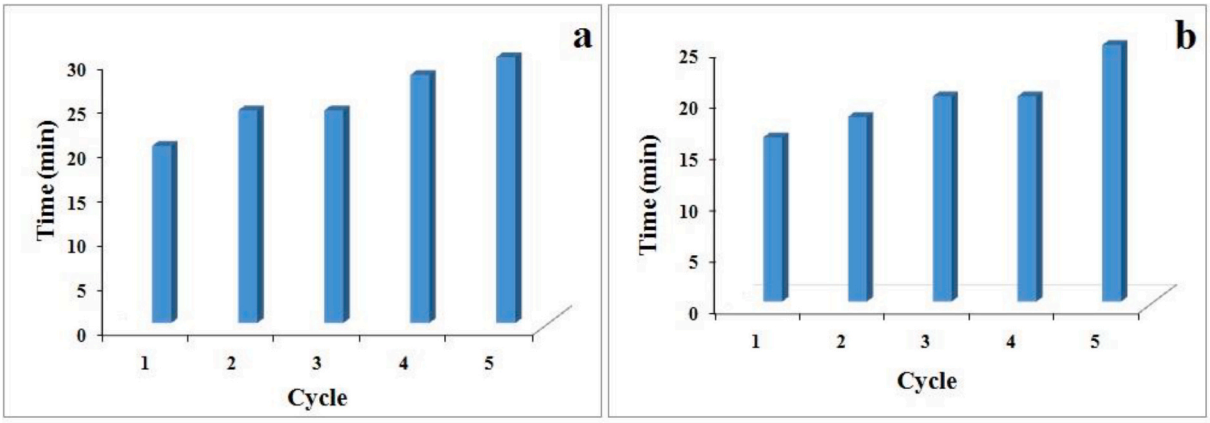


**Fig. 14.** Reusability studies of 4-NP reduction using a) AgNi/PC and b) AgNi/PC@Mn catalysts.

used, the reduction was completed in 20 min in the 1st cycle, while the reduction was completed in 30 min in the 5th cycle. Similarly, the reduction was completed in 16 min for the 1st cycle and in 25 min for the 5th cycle by using the AgNi/PC@Mn catalyst. Despite the increase in the time required for the complete reduction, a decrease in the efficiency of the catalysts could not be determined. The AgNi/PC@Mn catalyst obtained after the 5th run was investigated using the ICP technique. The contents of metal nanoparticles in the recycled catalyst for Ag, Ni, and Mn were 2.2 + 0.1, 1.2 + 0.1, and 0.6 + 0.01 wt%, respectively. ICP data show that metal leaching from the catalyst is negligible. It proves that AgNi/PC@Mn is very stable for nitrophenol reductions.

## 4. Conclusion

In this study, the synthesis of asphaltene-based porous carbon-supported bimetallic and trimetallic nanocatalysts containing Ag, Ni, and Mn elements for the catalytic reduction of nitrophenols was achieved for the first time. The chemical composition of the catalysts and successful incorporation of the NPs into the PC support were confirmed by XRD, EDX, and ICP-OES analysis. In addition to the EDX signals observed in AgNi/PC bimetallic nanoparticles, signals around 5.81 keV ($MnK_{\alpha}$) and 6.45 keV ($MnK_{\beta}$) for trimetallic nanoparticles supported the formation of trimetallic structures. The addition of Mn NP imparts thermal stability to the trimetallic catalyst, and the $N_2$ uptake value of 86 $cm^3/g$ was increased to 564 $cm^3/g$. The synthesized bi- and trimetallic catalysts exhibited excellent activity (~100% efficiency) and recyclability toward 4-NP reduction by $NaBH_4$. Higher catalyst loading caused a sudden increase in initial rate constants and a further reduction in time. It was determined that the reaction rate constants decreased with increasing 4-NP concentrations. Both catalysts remained active with an efficiency of ~100% in the 5th cycle. As a result, the designed PC-supported trimetallic catalysts exhibited valuable properties such as high stability, simple preparation, easy recovery/reusability, and excellent catalytic activity in reducing 4-NP due to their nanostructure and high surface area.

## Funding information

The Scientific Research Projects Coordination Unit of Kırıkkale University (Türkiye) (Project No. 2019/109 and 2021/074).

## CRediT authorship contribution statement

**Hikmet Beyza Erdem:** Investigation, Formal analysis, Data curation. **Sevil Çetinkaya:** Writing – review & editing, Supervision, Project administration, Funding acquisition, Data curation, Conceptualization.

## Declaration of competing interest

The authors declare that they have no known competing financial interests or personal relationships that could have appeared to influence the work reported in this paper.

## Data availability

Data will be made available on request.

## Acknowledgements

This work was supported by the Scientific Research Projects Coordination Unit of Kırıkkale University. (Project Number: 2019/109 and 2021/074).

## References


[1] M.I. Din, R. Khalid, Z. Hussain, T. Hussain, A. Mujahid, J. Najeeb, F. Izhar, Nanocatalytic assemblies for catalytic reduction of nitrophenols: a critical review, Crit. Rev. Anal. Chem. 50 (2020) 322–338, https://doi.org/10.1080/10408347.2019.1637241.

[2] P. Balasubramaniana, T.S.T. Balamurugana, S.M. Chena, T.W. Chena, Simplistic synthesis of ultrafine $CoMnO_3$ nanosheets: An excellent electrocatalyst for highly sensitive detection of toxic 4-nitrophenol in environmental water samples, J. Hazard. Mater. 361 (2019) 123–133, https://doi.org/10.1016/j.jhazmat.2018.08.070.

[3] A. Balakrishnan, G.J. Gaware, M. Chinthala, Heterojunction photocatalysts for the removal of nitrophenol: a systematic review, Chemosphere. 310 (2023) 136853, https://doi.org/10.1016/j.chemosphere.2022.136853.

[4] J. Fan, H. Wu, R. Liu, L. Meng, Y. Sun, Review on the treatment of organic wastewater by discharge plasma combined with oxidants and catalysts, Environ. Sci. Pollut. Res. 28 (2021) 2522–2548, https://doi.org/10.1007/s11356-020-11222-z.

[5] A. Goyal, S. Bansal, S. Singhal, Facile reduction of nitrophenols: comparative catalytic efficiency of $MFe_2O_4$ (M= Ni, Cu, Zn) nano ferrites, Int. J. Hydrogen Energy 39 (2014) 4895–4908, https://doi.org/10.1016/j.ijhydene.2014.01.050.

[6] U. Sanyal, D.T. Davis, B.R. Jagirdar, Bimetallic core–shell nanocomposites using weak reducing agent and their transformation to alloy nanostructures, Dalton Trans. 42 (2013) 7147–7157, https://doi.org/10.1039/C3DT33086A.

[7] T. Wi-Afedzi, E. Kwon, D.D. Tuan, K.A. Lin, F. Ghanbari, Copper hexacyanoferrate nanocrystal as a highly efficient non-noble metal catalyst for reduction of 4-nitrophenol in water, Sci. Total Environ. 703 (2020) 134781, https://doi.org/10.1016/j.scitotenv.2019.134781.

[8] S.S. Emmanuel, A.A. Adesibikan, O.D. Saliu, E.A. Opatola, Greenly biosynthesized bimetallic nanoparticles for ecofriendly degradation of notorious dye pollutants: a review, Plant Nano Biol. 3 (2023) 100024, https://doi.org/10.1016/j.plana.2023.100024.

[9] H. Akbarzadeh, E. Mehrjouei, M. Abbaspour, S. Salemi, H. Yaghoubi, M. Kamrani, Thermal behavior of different types of Au–Pt–Pd nanoparticles: dumbbell-like, three-shell, core-shell, and random-alloy, Mater. Chem. Phys. 294 (2023) 126955, https://doi.org/10.1016/j.matchemphys.2022.126955.

[10] A.Z. Medynska, M. Marchelek, M. Diak, E. Grabowska, Noble metal-based bimetallic nanoparticles: the effect of the structure on the optical, catalytic and photocatalytic properties, Adv. Colloid Interface Sci. 229 (2016) 80–107, https://doi.org/10.1016/j.cis.2015.12.008.

[11] R. Wei, R. Tang, L. Jiang, J. Yang, J. Guo, X. Yuan, J. Liang, Y. Zhu, Z. Wu, H. Li, Bimetallic nanoparticles meet polymeric carbon nitride: fabrications, catalytic applications and perspectives, Coord. Chem. Rev. 462 (2022) 214500, https://doi.org/10.1016/j.ccr.2022.214500.

[12] Z. Zang, Y. Wang, X. Wang, Nanoporous bimetallic Pt–Au alloy nanocomposites with superior catalytic activity towards electro-oxidation of methanol and formic acid, Nanoscale. 3 (2011) 1663–1674, https://doi.org/10.1039/C0NR00830C.

[13] R. Saha, D. Arunprasath, G. Sekar, Surface enriched palladium on palladium-copper bimetallic nanoparticles as catalyst for polycyclic triazoles synthesis, J. Catal. 377 (2019) 673–683, https://doi.org/10.1016/j.jcat.2019.07.063.

[14] C.S. Budi, J.R. Deka, D. Saikia, H.M. Kao, Y.C. Yang, Ultrafine bimetallic Ag-doped Ni nanoparticles embedded in cage-type mesoporous silica SBA-16 as superior catalysts for conversion of toxic nitroaromatic compounds, J. Hazard. Mater. 384 (2020) 121270, https://doi.org/10.1016/j.jhazmat.2019.121270.

[15] G. Sharma, D. Kumar, A. Kumar, H. Al-Muhtaseb Ala'a, D. Pathania, M. Naushad, G.T. Mola, Revolution from monometallic to trimetallic nanoparticle composites, various synthesis methods and their applications: a review, Mater. Sci. Eng. C. 71 (2017) 1216–1230, https://doi.org/10.1016/j.msec.2016.11.002.

[16] M. Liu, B. Niu, X. Chen, X. Lin, Z. Chen, H. Guo, One-step simple calcination of Ni@C(N) core-shell microspheres: catalytic reduction of 4-nitrophenol, supercapacitor and electrocatalytic hydrogen production, J. Alloys Compd. 937 (2023) 168467, https://doi.org/10.1016/j.jallcom.2022.168467.

[17] N. Basavegowda, T.K. Mandal, K.H. Baek, Bimetallic and trimetallic nanoparticles for active food packaging applications: a review, Food and Bioprocess Technol. 13 (2020) 30–44, https://doi.org/10.1007/s11947-019-02370-3.

[18] S. Liu, S. Yin, H. Zhang, S. Jiao, Z. Wang, Y. Xu, X. Li, L. Wang, H. Wang, Trimetallic Au@PdPt porous core-shell structured nanowires for oxygen reduction electrocatalysis, Chem. Eng. J. 428 (2022) 131070, https://doi.org/10.1016/j.cej.2021.131070.

[19] M. Duan, L. Jiang, G. Zeng, D. Wang, W. Tang, J. Liang, H. Wang, D. He, Z. Liu, L. Tang, Bimetallic nanoparticles/metal-organic frameworks: synthesis, applications and challenges, Appl. Mater. Today 19 (2020) 100564, https://doi.org/10.1016/j.apmt.2020.100564.

[20] A. Fakhri, S. Tahami, M. Naji, Synthesis and characterization of core-shell bimetallic nanoparticles for synergistic antimicrobial effect studies in combination with doxycycline on burn specific pathogens, J. Photochem. Photobiol. B 169 (2017) 21–26, https://doi.org/10.1016/j.jphotobiol.2017.02.014.

[21] J. Polte, Fundamental growth principles of colloidal metal nanoparticles-a new perspective, CrystEngComm 17 (2015) 6809–6830, https://doi.org/10.1039/C5CE01014D.

[22] B. Vanrenterghem, B. Geboes, S. Bals, J. Ustarroz, A. Hubin, T. Breugelmans, Influence of the support material and the resulting particle distribution on the deposition of Ag nanoparticles for the electrocatalytic activity of benzyl bromide reduction, Appl. Catal. Environ. 181 (2016) 542–549, https://doi.org/10.1016/j.apcatb.2015.08.026.

[23] B.E. Hayden, D. Pletcher, J.P. Suchsland, Enhanced activity for electrocatalytic oxidation of carbon monoxide on titania-supported gold nanoparticles, Angew. Chem. Int. Ed. Engl. 46 (2007) 3530–3532, https://doi.org/10.1002/anie.200604633.

[24] P. Sudhakar, H. Soni, Catalytic reduction of nitrophenols using silver nanoparticles-supported activated carbon derived from agro-waste, J. Environ. Chem. Eng. 6 (2018) 28–36, https://doi.org/10.1016/j.jece.2017.11.053.

[25] M.B. Kabataş, S. Çetinkaya, Petroleum asphaltene-derived highly porous carbon for the efficient removal of pharmaceutical compounds in water, J. Porous. Mater. 29 (2022) 1211–1224, https://doi.org/10.1007/s10934-022-01249-7.

[26] M. Kumar, S. Deka, Multiply twinned AgNi alloy nanoparticles as highly active catalyst for multiple reduction and degradation reactions, Appl. Mater. Interfaces 6 (2014) 16071–16081, https://doi.org/10.1021/am503913y.

[27] D. Chen, C. Han, Q. Sun, J. Ding, Q. Huang, T.T. Li, Y. Hu, J. Qian, S. Huang, Bimetallic AgNi nanoparticles anchored onto MOF-derived nitrogen-doped carbon nanostrips for efficient hydrogen evolution, Green Energy Environ. 8 (2023) 258–266, https://doi.org/10.1016/j.gee.2021.04.003.

[28] R. Dhanda, M. Kidwai, Reduced graphene oxide supported $Ag_xNi_{100-x}$ alloy nanoparticles: a highly active and reusable catalyst for the reduction of nitroarenes, J. Mater. Chem. A 3 (2015) 19563–19574, https://doi.org/10.1039/C5TA03779D.

[29] N. Bhandary, A.P. Singh, S. Kumar, P.P. Ingole, G.S. Thakur, A.K. Ganguli, S. Basu, In situ solid-state synthesis of a AgNi/g-$C_3N_4$ nanocomposite for enhanced photoelectrochemical and photocatalytic activity, ChemSusChem. 9 (2016) 2816–2823, https://doi.org/10.1002/cssc.201600740.

[30] Q.X. Wang, M.T. Yuan, H.Y. Shen, H.Y. Zhang, X. Chen, Y. Xu, X.X. Duan, K.L. Liu, T. Gao, Y.G. Ning, J. Wang, Fabrication of polyaniline-supported bimetal AgNi nanoparticles and the enhanced performance towards formate oxidation, J. Solid State Electrochem. 25 (2021) 1197–1205, https://doi.org/10.1007/s10008-021-04902-4.

[31] H.B. Erdem, S. Çetinkaya, Facile insitu preparation of silver nanoparticles supported on petroleum asphaltene-derived porous carbon for efficient reduction of nitrophenols, Heliyon. 8 (2022) e10659, https://doi.org/10.1016/j.heliyon.2022.e10659.

[32] D. Wu, D. Cheng, Core/shell AgNi/PtAgNi nanoparticles as methanol-tolerant oxygen reduction electrocatalysts, Electrochim. Acta 180 (2015) 316–322, https://doi.org/10.1016/j.electacta.2015.08.127.

[33] Y. Chen, D.L. Peng, D. Lin, X. Luo, Preparation and magnetic properties of nickel nanoparticles via the thermal decomposition of nickel organometallic precursor in alkylamines, Nanotechnol. 18 (2007) 505703, https://doi.org/10.1088/0957-4484/18/50/505703.

[34] G.T.K. Fey, C.L. Chen, High-capacity carbons for lithium-ion batteries prepared from rice husk, J. Power Sources 97 (2001) 47–51, https://doi.org/10.1016/S0378-7753(01)00504-3.

[35] M.S. Azarkhalil, K. Bahram, Synthesis of silver nanoparticles from spent X-ray photographic solution via chemical reduction, Iran. J. Chem. Chem. Eng. 35 (2016) 1–8,, https://doi.org/10.30492/ijcce.2016.22052.

[36] D.H. Chen, S.R. Wang, Protective agent-free synthesis of Ni–Ag core–shell nanoparticles, Mater. Chem. Phys. 100 (2006) 468–471, https://doi.org/10.1016/j.matchemphys.2006.01.027.

[37] V.G.B. Medrano, V. Nino-Celis, R.I. Giraldo, Systematic analysis of the nitrogen adsorption-desorption isotherms recorded for a series of microporous–mesoporous amorphous aluminosilicates using classical methods, ChemRxiv. (2022), https://doi.org/10.26434/chemrxiv-2022-8v4h3.

[38] M.S. Mrudula, N. Tiwari, S.N. Jha, D. Bhattacharyya, M.R.G. Nair, Structural studies on transition metal ion complexes of polyethylene oxide-natural rubber block copolymers, J. Polym. Res. 191 (2019) 191837, https://doi.org/10.1007/s10965-019-1837-y.

[39] T. Varadavenkatesan, R. Selvaraj, R. Vinayagam, Green synthesis of silver nanoparticles using Thunbergia grandiflora flower extract and its catalytic action in reduction of Congo red dye, Mater. Today Proc. 23 (2020) 39–42, https://doi.org/10.1016/j.matpr.2019.05.441.

[40] A.C. Lua, T. Yang, Effect of activation temperature on the textural and chemical properties of potassium hydroxide activated carbon prepared from pistachio-nut shell, J. Colloid. Interf. Sci. 274 (2004) 594–601, https://doi.org/10.1016/j.jcis.2003.10.001.

[41] M.Q. Doan, N.H. Anh, H.V. Tuan, N.C. Tu, N.H. Lum, N.T. Khi, V.N. Phan, P. D. Thang, A.T. Le, Improving SERS sensing efficiency and catalytic reduction activity in multifunctional ternary Ag-$TiO_2$ -GO nanostructures: roles of electron transfer process on performance enhancement, Adsorpt. Sci. Technol. 13 (2021) 1169599, https://doi.org/10.1155/2021/1169599.

[42] H. Liu, H. Xing, R. Shi, X. Ji, Facial synthesis of Al@$MnO_2$ with enhanced microwave absorption and low infrared emissivity, J. Mater. Sci.: Mater. Electron. 31 (2020) 18791–18802, https://doi.org/10.1007/s10854-020-04419-y.

[43] I. Djerdj, G. Garnweitner, D.S. Su, M. Niederberger, Morphology-controlled nonaqueous synthesis of anisotropic lanthanum hydroxide nanoparticles, J. Solid State Chem. 180 (2007) 2154–2165, https://doi.org/10.1016/j.jssc.2007.05.019.

[44] V.K. Harika, H.K. Sadhanala, I. Perelshtein, A. Gedanken, Sonication-assisted synthesis of bimetallic Hg/Pd alloy nanoparticles for catalytic reduction of nitrophenol and its derivatives ultrason, Sonochem. 60 (2020) 104804, https://doi.org/10.1016/j.ultsonch.2019.104804.

[45] N.C. Das, T.K. Das, Advances on catalytic reduction of 4-nitrophenol by nanostructured materials as benchmark reaction, Int. Nano Lett. 12 (2022) 223–242, https://doi.org/10.1007/s40089-021-00362-w.

[46] S. Gu, S. Wunder, Y. Lu, M. Ballauff, R. Fenger, K. Rademann, B. Jaquet, A. Zaccone, Kinetic analysis of the catalytic reduction of 4-nitrophenol by metallic

nanoparticles, J. Phys. Chem. C. 118 (2014) 18618–18625, https://doi.org/10.1021/jp5060606.
[47] S. Wunder, F. Polzer, Y. Lu, Y. Mei, M. Ballauff, Kinetic analysis of catalytic reduction of 4-nitrophenol by metallic nanoparticles immobilized in spherical polyelectrolyte brushes, J. Phys. Chem. C 114 (2010) 8814–8820, https://doi.org/10.1021/jp101125j.
[48] Z. Gong, T. Ma, F. Liang, Syntheses of magnetic blackberry-like Ni@Cu@Pd nanoparticles for efficient catalytic reduction of organic pollutants, J. Alloys Compd. 873 (2021) 159802, https://doi.org/10.1016/j.jallcom.2021.159802.
[49] S. Velpula, S.R. Beedu, K. Rupula, Biopolymer-based trimetallic nanocomposite synthesis, characterization and its application in the catalytic degradation of 4-nitrophenol, J Mater Sci: Mater Electron 33 (2022) 2677–2698, https://doi.org/10.1007/s10854-021-07476-z.
[50] K. Suwannarat, K. Thongthai, S. Ananta, L. Srisombat, Synthesis of hollow trimetallic Ag/Au/Pd nanoparticles for reduction of 4-nitrophenol, Colloids Surf. A Physicochem. Eng. Asp. 540 (2018) 73–80, https://doi.org/10.1016/j.colsurfa.2017.12.046.
[51] M.A. Malik, A.A. Alshehri, R. Patel, Facile one-pot green synthesis of ag–Fe bimetallic nanoparticles and their catalytic capability for 4-nitrophenol reduction, J. Mater. Res. Technol. 12 (2021) 455–470, https://doi.org/10.1016/j.jmrt.2021.02.063.
[52] N. Arora, A. Mehta, A. Mishra, S. Basu, 4-Nitrophenol reduction catalysed by Au-Ag bimetallic nanoparticles supported on LDH: Homogeneous vs. heterogeneous catalysis, Appl. Clay Sci. 151 (2018) 1–9, https://doi.org/10.1016/j.clay.2017.10.015.